Journal of the European Ceramic Society 44 (2024) 6827–6838

Contents lists available at ScienceDirect

Journal of the European Ceramic Society

journal homepage: www.elsevier.com/locate/jeurceramsoc

Mechanical properties of hafnium tantalum carbides via field assisted sintering technology for hypersonic vehicles

Patrick E. Albert [a,b,*], Caillin J. Ryan [a,b], Erik T. Furton [b], Ryan Sweny [a,b], Michael P. Galaini [a,b], Ryan J. Crealese [a,b], Petr A. Kolonin [a,b], Allison M. Beese [b,e], Douglas E. Wolfe [b,c,d]

[a] Applied Research Laboratory, The Pennsylvania State University, University Park, PA 16802, United States
[b] Materials Science and Engineering Department, The Pennsylvania State University, University Park, PA 16802, United States
[c] Engineering Science and Mechanics Department, The Pennsylvania State University, University Park, PA 16802, United States
[d] Ken and Mary Alice Lindquist Nuclear Engineering Department, The Pennsylvania State University, University Park, PA 16802, United States
[e] Department of Mechanical Engineering, The Pennsylvania State University, University Park, PA 16802, United States

ARTICLE INFO

Keywords:
Carbides
Mechanical properties
Ultra-high temperature ceramics
Field assisted sintering technology (FAST)
Hypersonics

ABSTRACT

Ultra-high temperature ceramics (UHTCs) are refractory transition-metal carbides, nitrides, and borides with the highest melting temperatures known materials, making them prime candidates for applications in aerospace and hypersonic vehicles. Of the UHTCs, tantalum carbide (TaC) and hafnium carbide (HfC) feature the highest melting temperatures. We investigated the binderless consolidation of HfC/TaC powder blends using Field Assisted Sintering Technology (FAST). Powders consisting of 90/10, 50/50, and 10/90 vol% HfC:TaC were sintered to high densities (>94 %). Bulk and nanomechanical, chemical, and microstructural characterization revealed substantially greater strength, hardness, and stiffness for ternary alloys. Mechanical properties correlated with physiochemical analysis indicated trace oxygen phases, solid-solution strengthening, and non-stoichiometric carbon were the key mechanisms driving the peak property enhancement of the 50 vol% solid-solution sample, despite lower densities. This study provides insight into optimizing the compositional design of HfC-TaC alloys by balancing influences from solid solution strengthening and the thermodynamic effects of oxygen/carbon stoichiometry.

1. Introduction

Materials capable of withstanding high temperatures are increasingly sought after as temperature-critical applications become more demanding, such as in hypersonic vehicles and aerospace leading edges [1–4]. In these applications, beyond the high melting point requirement, reliable mechanical strength is necessary to meet the needs of the harsh thermochemical and thermomechanical operating conditions [5–8]. These operating conditions require material systems that can withstand thermal shock-induced failure, which requires high strength, high toughness, low coefficient of thermal expansion, and high thermal conductivity [9–11].

The leading material candidates that meet these requirements are ultra-high temperature ceramics (UHTCs), which are a class of materials traditionally defined by their high melting points, generally greater than 3000 °C [12], composed of select transition metal carbides, nitrides, and borides [13,14]. The ternary solid solution of the TaC-HfC system boasts the highest experimentally measured melting temperatures, exceeding 3900 °C [15–18]. Furthermore, it has been predicted that tailoring the stoichiometry of $Ta_{0.8}Hf_{0.2}C$ can lead to the formation of an UHT-stable oxide phase ($Hf_6Ta_2O_{17}$) that may reduce oxygen diffusion rates and thus the rate of subsequent oxidation [17,19–21].

These promising attributes have prompted investigations exploring the synthesis of TaC-HfC ternary carbides by both traditional sintering [22,23] and melting techniques [24]. Densification of these compounds has proven challenging, as effective sintering of most compounds generally occurs between 50 % and 75 % of the material's homologous temperature [25]. Obtaining high density products with conventional sintering processes typically requires the use of sintering additives such as pure metals, borides, carbides, oxides, or disilicide compounds to improve the consolidation to near theoretical density [26,27]. However, these additives diminish the maximum operating temperature as they introduce lower melting temperature species and may provide additional failure mechanisms from phases detrimental to operation in harsh

---

* Corresponding author at: Applied Research Laboratory, The Pennsylvania State University, University Park, PA 16802, United States.
E-mail address: pja5158@psu.edu (P.E. Albert).

https://doi.org/10.1016/j.jeurceramsoc.2024.05.029
Received 21 December 2023; Received in revised form 3 May 2024; Accepted 13 May 2024

Table 1
Nominal compositions of specimens studied.

HfC vol%	Ta		Hf		C	
	(wt%)	(at %)	(wt%)	(at %)	(wt%)	(at %)
0 %	93.8 %	50.0 %	-	-	6.2 %	50.0 %
10 %	85.8 %	45.7 %	8.0 %	4.3 %	6.2 %	50.0 %
50 %	50.9 %	27.0 %	42.8 %	23.0 %	6.3 %	50.0 %
90 %	10.9 %	5.8 %	82.8 %	44.2 %	6.3 %	50.0 %
100 %	-	-	93.7 %	50.0 %	6.3 %	50.0 %

environments. Therefore, manufacturing the aforementioned UHTCs into components with high-density, without the use of sintering aids or dopants, is highly desirable.

Field assisted sintering technology (FAST) is a manufacturing method capable of fabricating dense parts through the application of direct current, pressure, and high temperature. Through increased heating rates, exceeding 100 °C/min, compared to traditional sintering methods, FAST results in increased densification rates without accompanying grain growth [12,28–37]. Furthermore, FAST processes can occur at temperatures as high as 2400 °C, allowing for the necessary diffusion rates in combination with high compressive stresses up to 100 MPa to promote densification [38]. Previous efforts by Wolfe et al. have shown the capability to fabricate nearly-dense tantalum carbide (TaC), hafnium carbide (HfC), and their ternary phase (TaC-HfC) with FAST without sintering aids [39].

In this study, HfC-TaC samples were processed via FAST across various HfC contents under identical processing parameters, and microstructurally analyzed using XRD and SEM-EDS. Mechanical properties of strength, stiffness, and hardness were evaluated across various both macro and nano lengths scales by combining insights from three-point flexure testing and nanoindentation. The solid solution ternary HfC-TaC compositions demonstrated substantial synergistic improvements for both the bulk and nanomechanical properties when compared to properties calculated using the rule of mixtures with the TaC and HfC endmembers. This is correlated to enhanced bonding evident from the observed negative Vegard's law deviations. Furthermore, it was found that the complex interplay between thermodynamically driven changes in carbon and oxygen stoichiometry had influenced both phase stability and the resulting mechanical properties.

2. Experimental approach

2.1. Materials and powder processing

Tantalum carbide powder (14.5 g/cm^3) with 99.5 % purity and particle size of 1–3 μm was purchased from Stanford Advanced Materials (Irvine, CA; lot ID: OC200713–10365). The hafnium carbide powder (12.2 g/cm^3) (Reade Advanced Materials, Newton, MA) had a purity of 99 % with a quoted and experimentally measured average particle diameter between 1 μm and 3 μm [39]. Five compositions were explored in this study: two binary 0/100 and 100/0, and three ternary solid solution compositions of 10/90, 50/50, 90/10 vol% HfC:TaC (Table 1). For the HfC-TaC mixture, a 3:1 milling media (8 mol % yttria-stabilized zirconia, Inframat, Manchester, CT) to powder ratio was used to blend the three compositions in a Nalgene plastic jar; the powders occupied approximately half the volume. The powders were blended in a dry environment for 24 hours on the jar rolling mill. The milling conditions were chosen to minimize media contamination and preserve the phase and compositional purity of the blended powders. Powders were separated from the media using sieves.

Table 2
Number of mechanical test samples, where samples containing large, macroscopic defects were excluded from further analysis.

HfC vol%	Full-Sized		Half-Sized	
	Included	Excluded	Included	Excluded
0 %	1	2	5	1
10 %	3	0	6	0
50 %	3	0	6	0
90 %	2	1	4	2
100 %	3	0	6	0

2.2. FAST processing

The ceramic powders were consolidated into test coupons using a using a 25 Ton FAST system (FCT Systeme GmbH, Frankenblick, Germany). The test coupons were fabricated in a 40 mm outer diameter (OD) graphite die, where the final geometry was a 40 mm OD pellet with a thickness of approximately 5 mm. The internal faces of the die body at the powder-die interface were lined with graphite foil (0.38 mm) to minimize die degradation as a result of powder reactivity with the graphite die and to seal the powder in the assembly. All of the FAST trials were carried out under vacuum with a base pressure between 600 and 1000 Pa. The samples were heated at a rate of 100 °C/min from room temperature to their soak temperature of 2100 °C. Unlike previously published work exploring various processing conditions [39], identical processing conditions were used for all compositions to isolate compositional and microstructural effects on performance. The sintering process was a two-step process, where soak temperatures were 2100 and 2400 °C, pressures were 55 and 30 MPa, and hold times were 30 and 20 minutes, respectively. After sintering, the samples were removed from the die set and grit blasted with 100 grit aluminum oxide to remove residual graphite foil. Density was measured using the Archimedes method on a digital analytical balance (HM–202, ± 0.1 mg, A&D, Tokyo, Japan) after grit blasting, but prior to any mechanical grinding or removal of any carbide rich surface regions on the sample due to contamination from the graphite foil and die assembly.

2.3. Analytical materials preparation and characterization

The outer surfaces of the ceramics were encased in a carbon-rich layer from the graphite foil carburization at elevated temperatures, which were removed by grinding (220 grit diamond) to expose the HfC-TaC ceramic. The crystallinity of the sintered carbides was analyzed by X-ray diffraction (XRD) on the grinded faces for phase analysis identification. XRD analysis (Empyrean III, Malvern Panalytical, Malvern, United Kingdom) using Bragg-Brentano geometry was performed over a 2θ range of 20–80° (0.01 °/step, 2.5 s/step). An operating voltage of 40 kV and current of 45 mA were used at a beam wavelength of 1.5406 Å (CuKα with Ni filter). Phase identification was performed using the major intensity peaks in JADE software (MDI, Livermore, CA).

The morphologies, microstructures, planimetric grain sizes [40], and microstructural analysis were obtained from scanning electron microscope (SEM) measurements (Verios G4, ThermoFisher Scientific, Waltham, MA) and energy dispersive spectroscopy (X-Max, Oxford Instruments, Abingdon, United Kingdom). Carbon and oxygen contents were measured with combustion-infrared absorbance [41] and inert gas fusion [42] (IMR Test Labs, Lansing, NY). Thermodynamic modeling with the CALPHAD (CALculation of PHAse diagrams) approach (Thermo-Calc 2016b, Stockholm Sweden) with a tantalum-hafnium-carbon database [18] was used to calculate the solubility limit of carbon in the tantalum-hafnium matrix.

2.4. Mechanical property testing

Sintered samples were cross-sectioned using a diamond-coated wafering blade with a diameter of 127 mm into 3 × 5 × 35 mm bars and polished to a mirror-finish using a final 1 μm diamond suspension. Mechanical testing was conducted with an electromechanical load frame (Model 43, MTS, Eden Prairie, MN) with a bend length of 30 mm and a crosshead displacement rate of 0.005 mm/s, with an approximate strain

Table 3
Calibrated Weibull parameter values for HfC-TaC samples.

HfC vol%	σ_0 (MPa)	m (dimensionless)
0 %	319	6.1
10 %	385	34
50 %	403	19
90 %	390	18
100 %	370	19

rate of $1 \times 10^{-4}\ s^{-1}$. After fracture, to increase the amount of mechanical test data, the two fractured halves were subsequently mechanically tested with bend lengths of 15 mm. Due to the localized nature of fracture in a three-point bending test, there was no detectable damage carried over from the initial fracture test in the half-sized samples.

Optical microcopy (VHX-2000, Keyence, Osaka, Japan) identified which sample's cross-sections contained large, macroscopic processing defects, and those samples were excluded from further analysis. The number of excluded samples is shown in Table 2. The remaining 6–9 strength measurements were used to estimate Weibull parameters, fitting the distribution to the two-parameter Weibull distribution, which assumes failure being controlled by one population of flaw size:

$$f(\sigma) = \left(\frac{m}{\sigma_0}\right)\left(\frac{\sigma}{\sigma_0}\right)^{m-1} e^{-KV\left(\frac{\sigma}{\sigma_0}\right)^m} \tag{1}$$

where m is the Weibull modulus, σ_0 the characteristic strength, V the sample's volume, and K a geometric factor. Weibull statistics account for reduced strength for larger samples due to a greater probability that it contains a large flaw. Large values of m are indicative of narrow distributions of strength, where values between 5 and 20 are typical of engineering ceramics [43]. In three-point bending, the geometric factor, K, is $\frac{1}{2(m+1)^2}$ for flaws randomly distributed across the volume [44]. The best-fit Weibull parameters for each composition are provided in Table 3.

To limit the effect of differences in sample sizes between full-sized and half-sized test specimens, the Weibull distribution was used to convert all measured mechanical strengths ($\sigma_{Measured}$), corresponding to a given probability of failure, of samples with size V_{sample} to strengths of a reference sample (σ_{Ref}) with dimensions of $3\times5\times30\ mm^3$ for the same probability of failure as:

$$\sigma_{Ref} = \left(\frac{V_{sample}}{V_{ref}}\right)^{1/m} \sigma_{Measured} \tag{2}$$

The full sized-samples had similar sizes to the reference sample and thus similar reported strengths. Although the half-sized samples were measured (σ_{Sample}) to have a mean strength 8 % greater than the full-sized samples, once the size-effect was accounted for, the difference was only 3 %.

For nanomechanical property characterization, nanoindentation with a Berkovich tip (Hysitron TI-980, Bruker, Billerica, MA) was performed on the relative centers of mounted and polished HfC-TaC cross-sections. For high resolution indentations, indents were spaced in a 5×5 square grids with 5 μm spacing with 5 mN load for each sample. The loading profiles for the indents were quasi-static (QS) trapezoids, with 5-second loading/unloading times and 2-second hold times, where the hardness was measured using the Oliver-Pharr method [45]. In addition, these quasi-static trapezoid profiles were subsequently scanned with *in-situ* scanning probe microscopy (SPM) to confirm the validity of the nanoindents. An additional set of indents with analogous parameters (15×15 spaced 5 μm at 5mN, 0.5–0.2–0.5 s profile) was applied using the accelerated-property mapping (XPM) mode and complemented the quasi-static (QS) mode results to confirm observed trends. Between each sample, fused quartz calibrations and tip cleanings were routinely performed. After collection, all measured hardness values and force-displacement loading/unloading curves were screened for defects and outliers (i.e., curve discontinuities or abnormal profiles) before further analysis. The reduced modulus, which removes the compliance of the indenter tip from the stiffness measured by nanoindentation, was calculated using an indenter elastic modulus of the 1140 GPa and Poisson ratio of 0.07, and the Poisson ratio of the samples were obtained from density functional theory (DFT) simulations performed by Kim et al. [45,46].

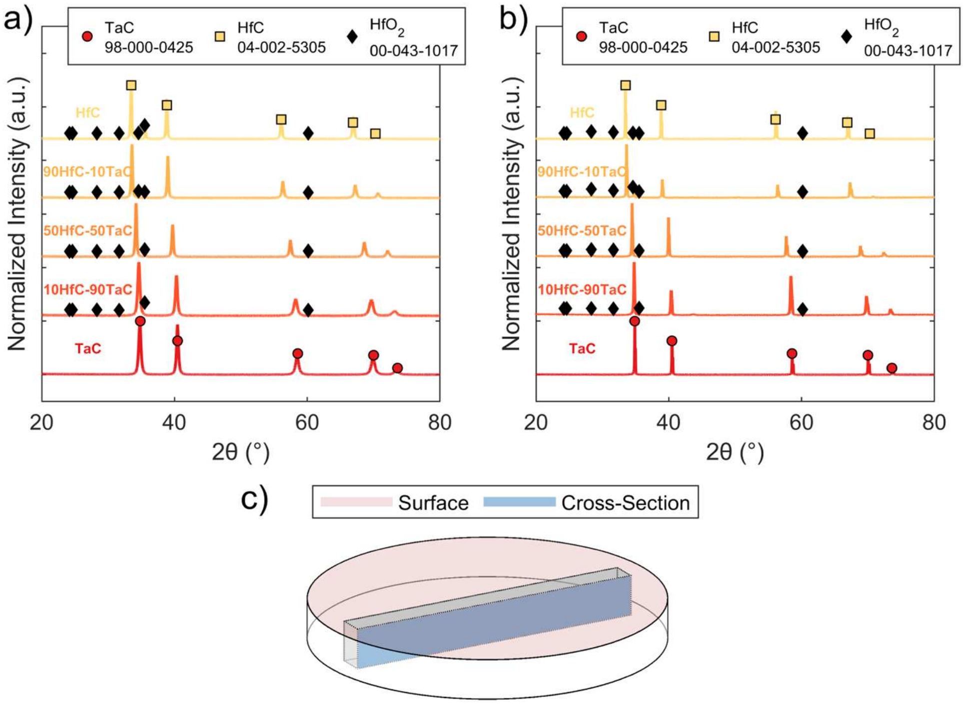

Fig. 1. X-ray diffraction comparison of the (a) surface region and (b) cross-sectional region of HfC-TaC FAST sintered pellets, and (c) schematic of surface and cross-sectional regions used for XRD.

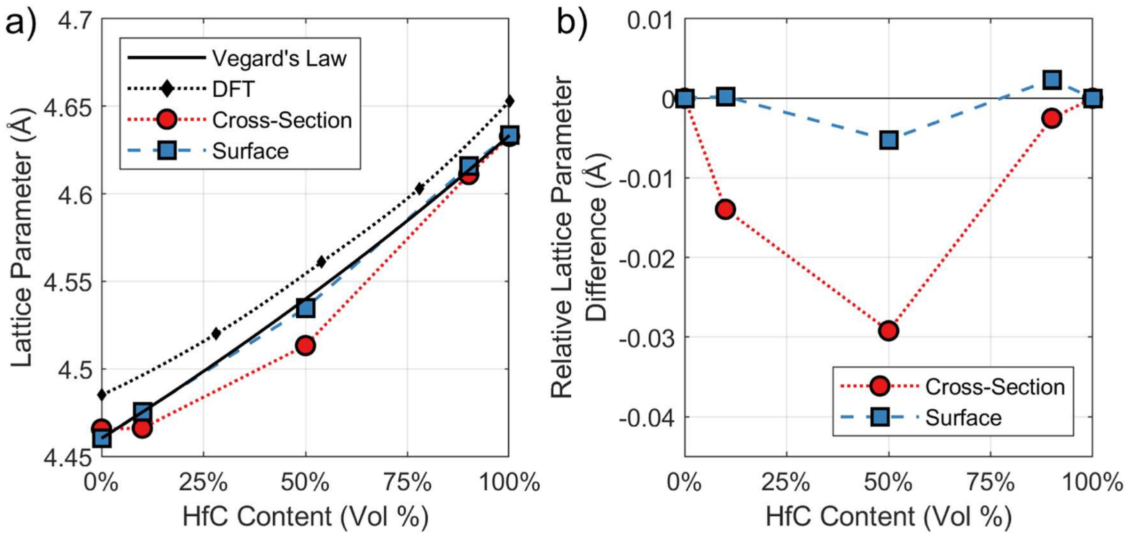

Fig. 2. (a) HfC-TaC lattice parameters measured at the cross-section and surface, compared to Vegard's Law and density function theory from Kim et al. [46] (b) Difference between measured XCT lattice spacing, predicted by Vegard's law. All plotted values are averages.

Table 4
Measured oxygen and carbon content, from inert gas fusion and combustion-infrared absorbance, in terms of atomic fraction. The designed compositions are in parentheses. The tantalum and hafnium fractions were calculated as at the remaining mass (not carbon or oxygen), at the sample's nominal ratio.

HfC vol%	Ta	Hf	C	O
0 %	49.80 % (50.0 %)	0.00 % (0.00 %)	49.96 % (50.00 %)	0.24 % (0.00 %)
10 %	45.49 % (45.67 %)	4.33 % (4.33 %)	48.88 % (50.00 %)	1.32 % (0.00 %)
50 %	25.65 % (26.99 %)	21.86 % (23.01 %)	47.90 % (50.00 %)	4.60 % (0.00 %)
90 %	5.51 % (5.77 %)	42.27 % (44.23 %)	45.03 % (50.00 %)	7.19 % (0.00 %)
100 %	0.00 % (0.00 %)	46.81 % (50.00 %)	43.54 % (50.00 %)	9.65 % (0.00 %)

3. Results and discussion

3.1. Characterization

X-ray diffraction measurements of the processed HfC-TaC ternary alloys are shown near the surface (Fig. 1*a*) and for a cross-section (Fig. 1*b*), and verify the presence of predominantly single phase solid solutions. A schematic of the two surfaces is shown in Fig. 1*c*. Increasing HfC content leads to smaller peak angles associated with larger lattice parameters from the incorporation of Hf atoms. Trace hafnia from the hafnium carbide source powder was detected in the blended mixtures for both regions, while no Ta_2C or Ta_2O_5 peaks were detected. The changes in peak height and breadth are indicative of differences in crystallinity of these regions, possibly caused by differences in crystallite size, texture, stoichiometry, or defect concentration.

The lattice parameters, calculated from the 5 peaks between 20° to 80° 2θ are shown in Fig. 2*a* as a function of HfC content, and are compared to those calculated by Vegard's mixing law. Although the near-surface lattice parameters closely follow those expected by Vegard's law, the cross-sections show a systematically negative

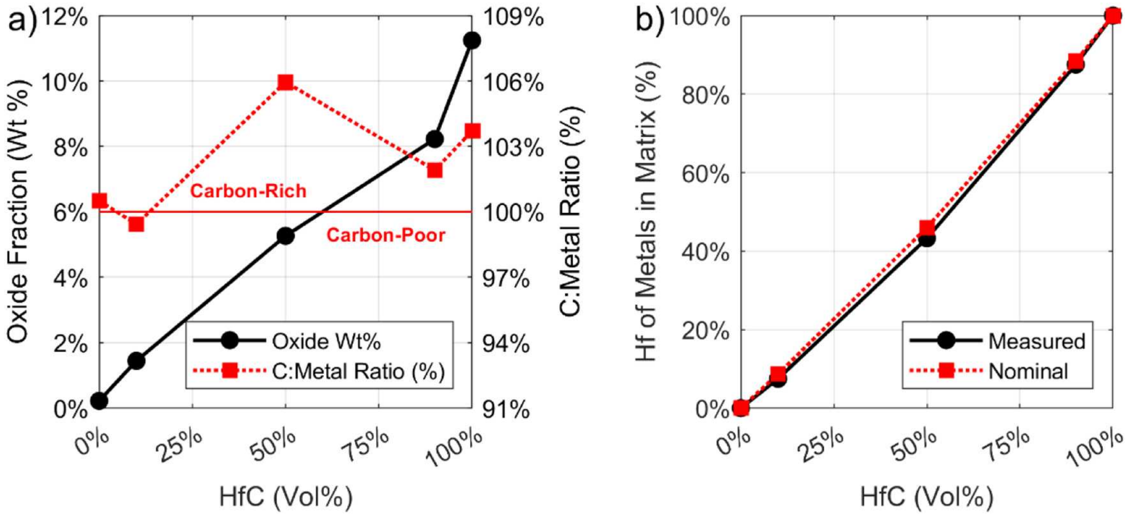

Fig. 3. (a) Oxide weight fraction (left-axis) and ratio of carbon to metal in the (Ta,Hf)C rocksalt phase (right-axis). (b) In the matrix, the hafnium fraction is lower than anticipated due to the preferential formation of hafnia to tantalum oxide.

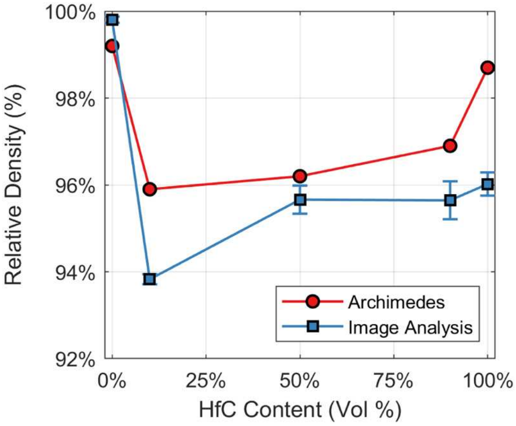

Fig. 4. Comparison of HfC-TaC densities from the Archimedes method and from image analysis of SEM micrographs.

deviation. Compared to DFT calculations from Kim et al. [46], the lattice parameters are smaller for all compositions. This difference may be attributed to both non-stoichiometric carbon and to the presence of contaminants such as oxygen, both of which reduce the lattice parameter [47,48].

The differences between the measured lattice parameters and Vegard's law are shown in Fig. 2*b*. The difference, suggesting stronger bonding, is greatest for 50TaC-50HfC, and is significantly greater for the cross-section than near the surface. The smaller lattice parameters near the surface compared to those of the cross-section are attributed to differences in oxygen content and carbon vacancies; as previously mentioned, carbon vacancies and dissolved oxygen are known to contract the lattice. Because the sample surface is directly in contact with graphite, the greater extent of carburization for the surface relative to the bulk cross-section led to annihilation of carbon vacancies with diffusing carbon atoms and reduced oxygen content with CO_x evolution. Hence, regional anion variations caused by the carbon foil in FAST lead to variations in lattice spacing.

The measured carbon and oxygen contents, using combustion-infrared absorbance and inert gas fusion, for samples after fabrication

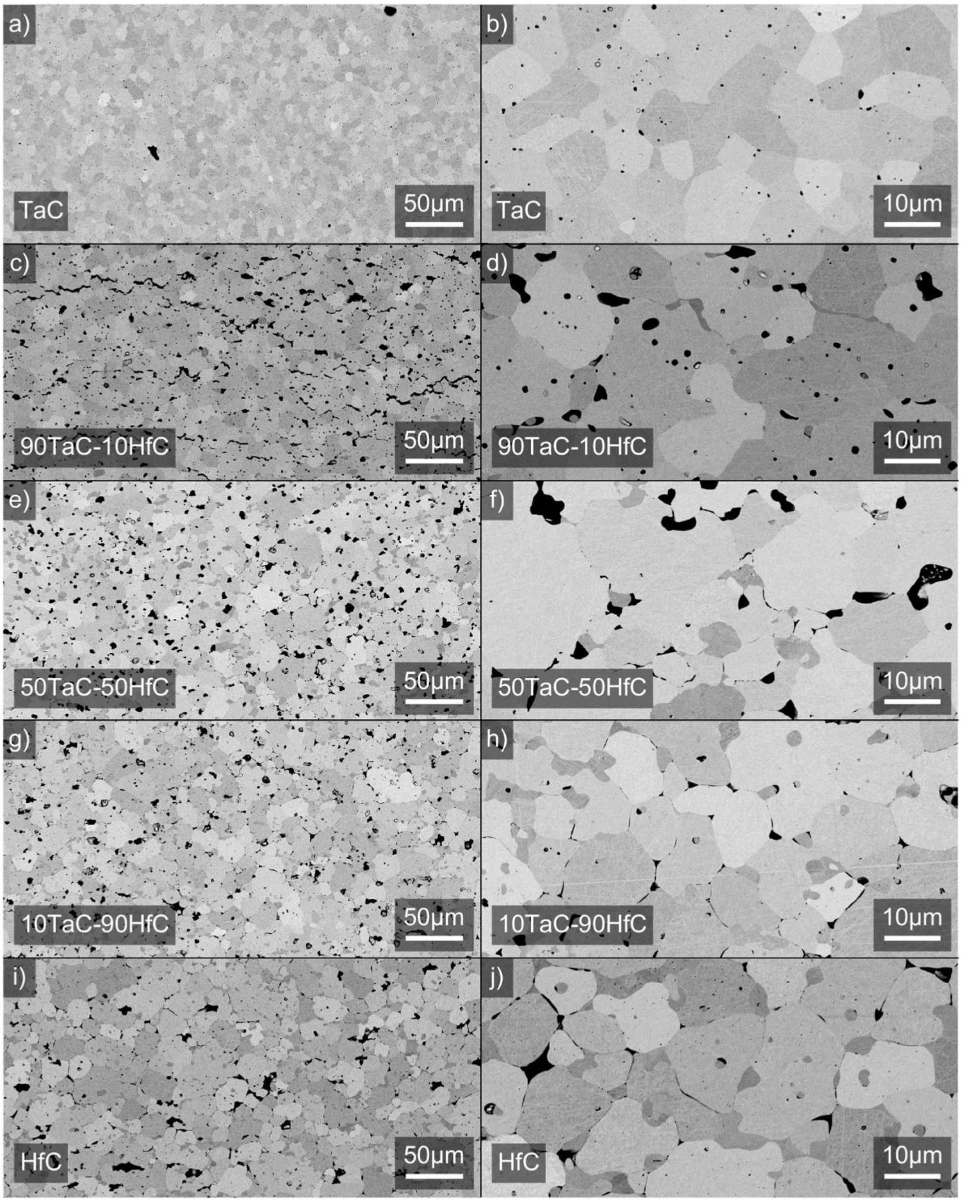

Fig. 5. SEM cross-sectional micrographs for a-b) TaC, c-d) 90TaC-10HfC, e-f) 50TaC-50HfC, g-h) 10TaC-90HfC, and i-j) HfC samples.

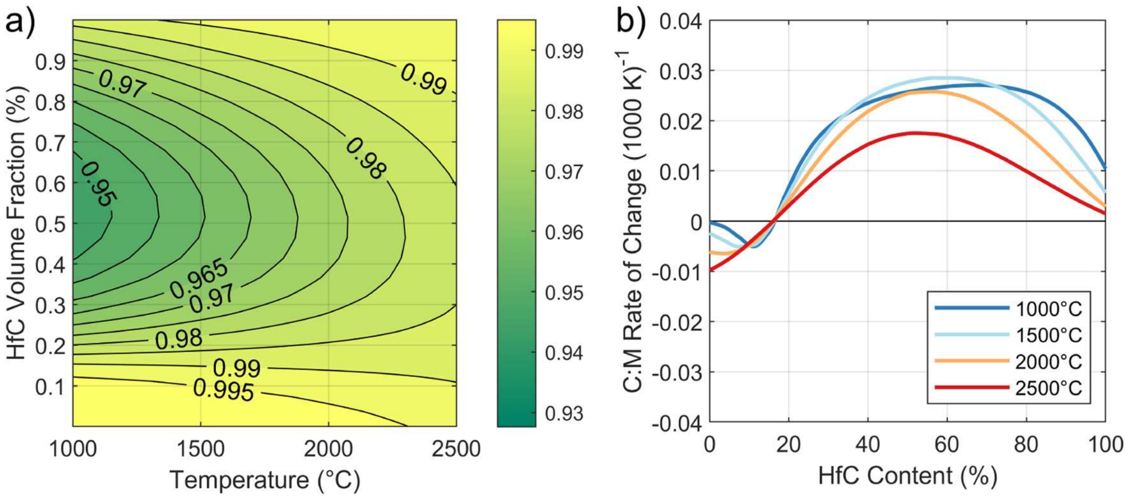

Fig. 6. (a) Contours of maximum equilibrium carbon-to-metal ratio as function of temperature and HfC volume fraction, calculated by using the thermodynamic database from Pan et al. [18] (b) Rate of change of carbon to metal ratio with respect to temperature, where positive values correspond to carbon being driving from the matrix during cooling, and conversely, negative values representing materials where carbon is absorbed by the matrix during cooling.

are shown in Table 4. With increasing HfC ratio, the oxygen content increases. Hafnium has a stronger affinity to oxygen than tantalum, and therefore all samples contain hafnia except for the pure tantalum sample. If all the oxygen is trapped in stoichiometric oxide phases (HfO_2 and Ta_2O_5), the weight fraction of oxides is shown in Fig. 3*a*, and it increases from 0.2 wt% to 11.2 wt% from TaC to HfC. Therefore, for HfC containing samples, the presence of HfO_2 is a key secondary phase. After accounting for the metal trapped in the oxide phases, the carbon-to-metal ratio is shown on the right-hand axis of Fig. 3*a*. For compositions containing mostly TaC, the ratio is near 1:1, whereas the sample is carbon-rich for samples with high HfC content. The greatest carbon-to-metal ratio exists for the intermediate TaC-HfC composition, where the ratio of carbon to metal not trapped in an oxide phase is 1.06:1. Although the rocksalt phase in the TaC-HfC system can be stable with sub-stoichiometric carbon, when the carbon-to-metal ratio exceeds unity, free carbon is thermodynamically favorable.

Because HfO_2 preferentially forms to Ta_2O_5, and because neither XRD nor EDS suggested the presence of $Hf_6Ta_2O_{17}$, the (Ta,Hf)C rocksalt phase contained less hafnium than intended. When hafnium in the oxide phase is excluded, the remaining hafnium fraction of metallic species in the (Ta,Hf)C phase is shown in Fig. 3*b*. The difference between the measured and designed hafnium content is minimal, never exceeding 3 %.

The Archimedes density and the dense area fraction calculated from

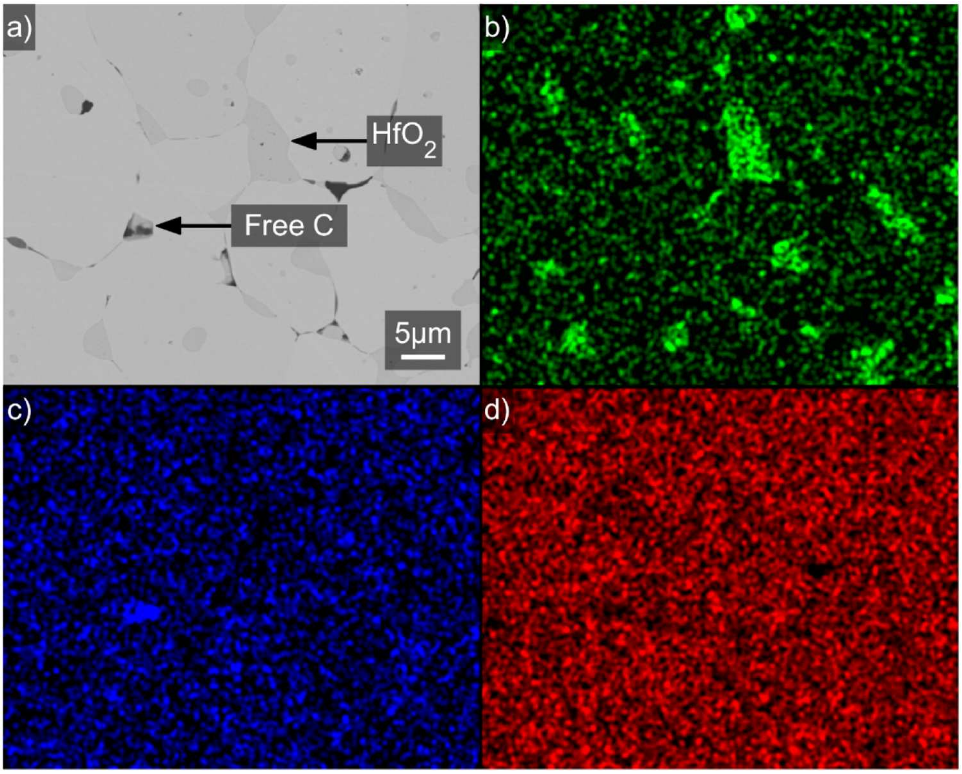

Fig. 7. HfC cross-sectional fracture surface micrographs with (a) SEM, (b) O elemental mapping, (c) C elemental mapping, and (d) Hf elemental mapping.

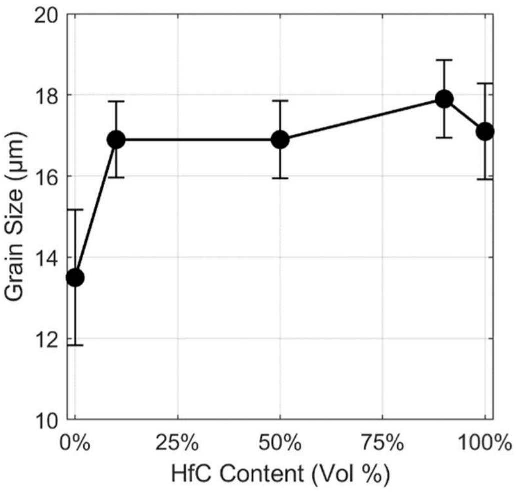

Fig. 8. HfC-TaC microstructural comparison of planimetric mean grain size, where error bars represent 95 % confidence intervals.

SEM micrographs are shown in Fig. 4. For the Archimedes method, the density of the fully-dense ternary compounds was assumed to be a linear combination of the end members. Discrepancies between the Archimedes and SEM density measurements may be attributed to the presence of oxides and carbon rich surface of the pellet prior to mechanical grinding and removal. The TaC endmember is approximately fully dense (>99 %), while the HfC endmember is the second densest, but is considerably lower than TaC. The presence of oxides limits the densification rate for HfC-containing members [49].

The relative density is lower for the ternary alloys compared to the endmembers. Because all samples were fabricated using the same time-temperature history, this can be attributed to the sluggish diffusion effects of stronger interactions in the lattice, as previously observed with the negative deviations from Vegard's law in Fig. 2, and from the presence of oxide species [49].

The cross-sectional microstructures are shown in Fig. 5. The pure TaC sample (Fig. 5*a*-*b*) is nearly dense, containing only scattered, circular pores inside grains, and no secondary phases are visible in the SEM micrographs or XRD (Fig. 1).

At 1720 °C, which is considerably below the processing temperature, Ta_2O_5 reacts with TaC to produce Ta_2C and carbon monoxide [50]. However, in the XRD patterns (Fig. 1), no trace amounts of Ta_2C were detected; Ta_2C may be challenging to detect, because upon cooling below 1100 °C, it undergoes metastable transformations [51]. Therefore, any oxygen present in the material prior to processing is eliminated under typical FAST processing parameters.

In Fig. 6*a*, the maximum carbon-to-metal ratio is shown as a function of HfC volume fraction and temperature. For pure TaC, during cooling, the solubility of carbon increases. The rate of change of carbon-to-metal ratio with respect to temperature is shown in Fig. 6*b*. For pure TaC, the rate is negative, indicative of a driving force for the rocksalt TaC phase to absorb carbon upon cooling. The measured C:Ta ratio is nearly unity (Fig. 3*a*), and SEM did not reveal any free carbon at grain boundaries. Therefore, without significant secondary phases or carbon at grain boundaries, the TaC samples were nearly pure.

For the HfC sample (Fig. 5i-j), the microstructure contains long pores that occupy 4 % of the cross-sectional area (Fig. 4). The pores are characteristic of intermediate sintering, where densification is not complete and pores are located at triple boundaries. Additionally, HfO_2 particles are found at grain boundaries. HfO_2 does not decompose or melt until 2800 °C [52], which exceeds the maximum processing temperature of 2400 °C in this study; therefore, unlike the TaC samples studied, the oxygen in the HfC-containing samples remained during processing. For the HfC sample, during the cooling process, the solubility of carbon in the matrix decreases, resulting in a driving force for free carbon to deposit at grain boundaries (Fig. 6*b*). This is evident in the high carbon concentration for pores when imaged in EDS in Fig. 7; with a C:M ratio of 1.04 (Fig. 3*b*), free carbon is thermodynamically stable.

For the ternary compositions, the porosity is between 4 % and 6 %

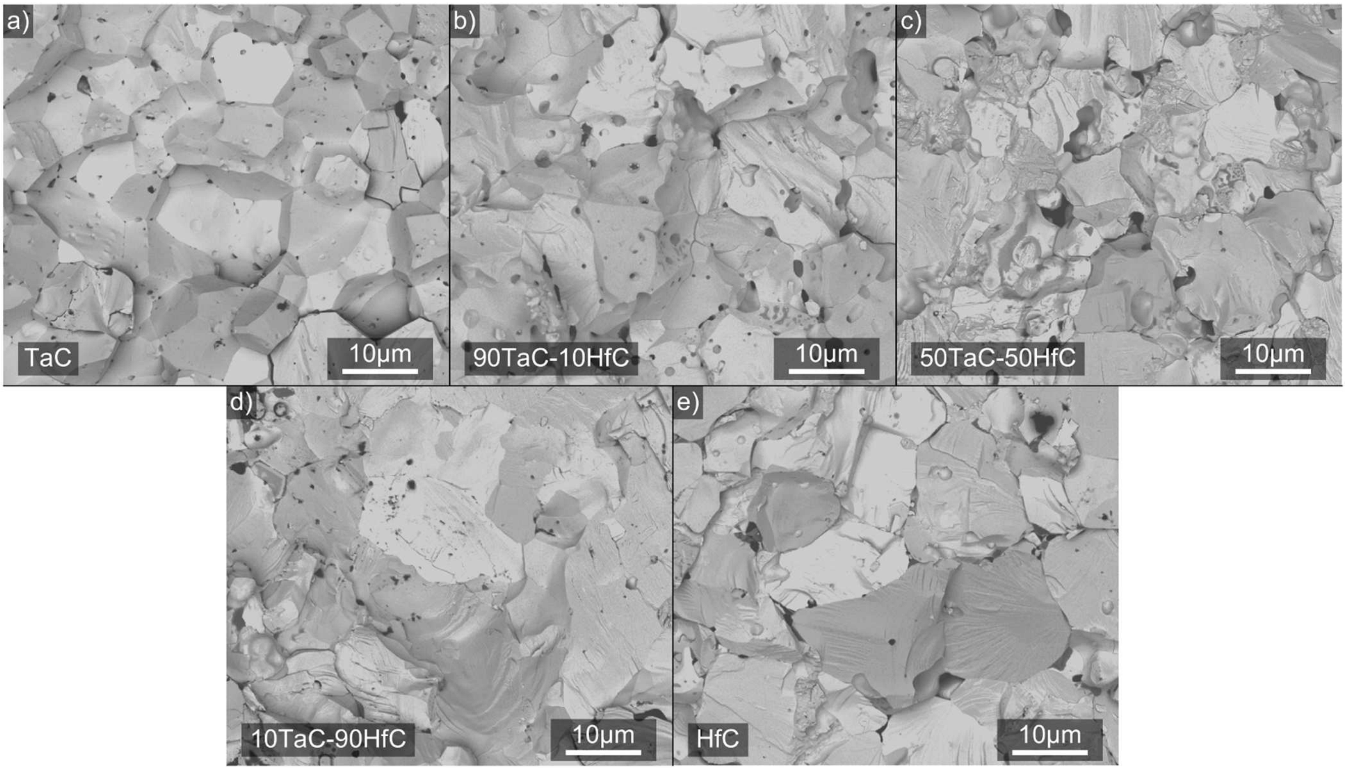

Fig. 9. SEM micrographs of fracture surface for (a) TaC, (b) 90TaC-10HfC, (c) 50TaC-50HfC, (d) 10TaC-90HfC, and (e) HfC samples.

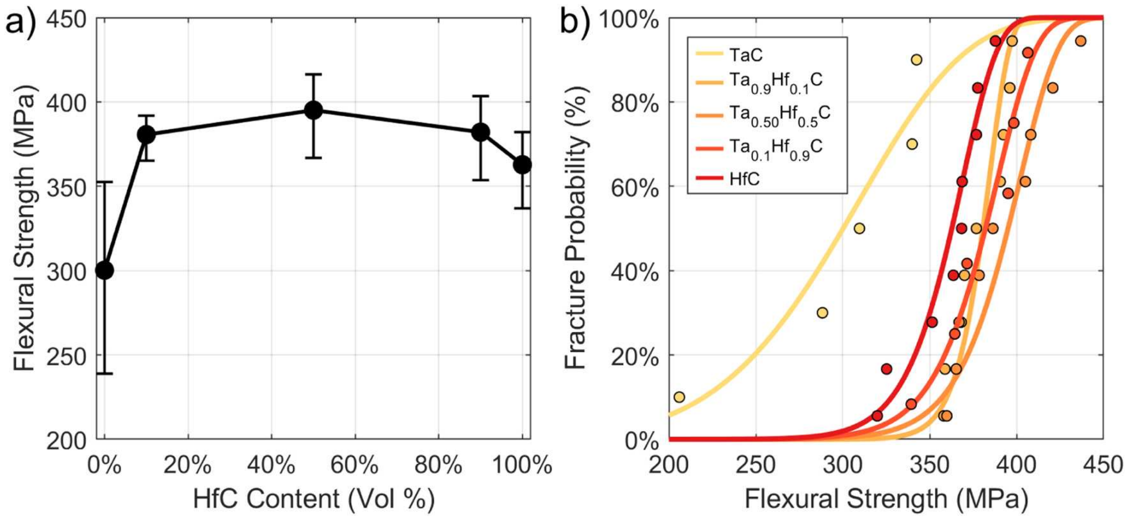

Fig. 10. Mechanical flexure testing comparison of HfC-TaC (a) flexural strength and (b) cumulative fracture probability fit with Weibull distributions. The markers in (a) represent median strength values and the error bars represent confidence intervals between 16 % and 84 %, calculated from the Weibull distributions, while the markers in (b) represent the strength from individual mechanical tests.

(Fig. 4), and pore morphologies are typical of the intermediate stage of sintering. No $Hf_6Ta_2O_{17}$ peaks were found in the XRD patterns (Fig. 1). As the concentration approached equal amounts of TaC to HfC, the driving force for carbon expulsion is greatest (Fig. 6*b*).

The mean grain sizes are compared in Fig. 8. The HfC-containing compositions have slightly larger grains than the TaC endmember, which is denser and contains less oxygen. This is consistent with reports of increased grain coarsening rate at the expense of densification due to the presence of oxygen [49]. The grain sizes for the ternary compositions are similar to those of the HfC endmember.

SEM micrographs of the fracture surfaces are shown in Fig. 9. For the TaC endmember (Fig. 9*a*), the fracture mode is intergranular. The HfC endmember's fracture surface contains both transgranular and intergranular features. The ternary members primarily contain transgranular features, despite the presence of oxides and free carbon at grain boundaries.

3.2. *Mechanical behavior*

The median flexural strength for each composition is shown in Fig. 10*a*. Despite the lower densities for ternary samples (Fig. 4), those samples had greater strength than the endmembers. Furthermore, the TaC samples which had the smallest grains, least porosity, and least oxygen contamination had the lowest flexural strength.

The flexural strength data were used to fit two-parameter Weibull distributions, shown in Fig. 10*a,* that describe the probability of failure. Although it is recommended for qualification purposes to use larger numbers of samples to estimate Weibull parameters [53], the number of samples studied here were sufficient to make qualitative comparisons between compositions. The TaC samples, in addition to being substantially weaker than the other compositions, had the widest distribution of strength, which is consistent with the intergranular fracture mode seen in Fig. 9*a*. The addition of 10 % HfC increased the median strength from 300 to 380 MPa. For all other compositions which contain hafnia and expel carbon from the (Ta,Hf)C rocksalt phase during cooling, the Weibull modulus was approximately 20, which is a narrow distribution for engineering ceramics [54].

The cause for the enhanced strength for the ternary compositions in flexural testing was investigated at smaller length scales with nanoindentation. In Fig. 11*a-b*, the nanohardness shows the material's resistance to localized plastic deformation, and is the greatest for compositions approaching 50/50 vol% HfC-TaC, with compositions containing HfC were more resistant than those containing predominantly TaC. The reduced modulus in Fig. 11*c-d* measures the stiffness of the sample, accounting for indenter compliance. Compared to density functional theory (DFT)-based calculations by Kim et al. [46], this study's TaC sample has considerably lower reduced modulus. The DFT-based predictions anticipate stiffness to monotonically decrease with added HfC content, while in this study, the reduced modulus was greatest for the 50/50 vol% composition. For samples containing at least 50 % HfC, the measured stiffness was greater than that calculated by DFT, implying that other mechanisms, such as carbon vacancies and dissolved oxygen, may have potentially increased the stiffness.

Consistency between the QS and XPM indentation modes and the parametric and nonparametric analysis demonstrate self-consistency in these observed trends, regardless of the probed area, resolution, or loading rates applied for indentation. This is indicative of an intrinsic hardening mechanism operant across the bulk material. If strengthening was caused by secondary phases or grain boundaries, the distribution of nanohardness and reduced modulus would be bimodal.

To evaluate the homogeneity of the strengthening mechanisms across the microstructure, the 3rd and 4th normalized moments of the measured data are shown in Fig. 12*a-b*, respectively. With increased HfC content, the nanohardness data became increasingly negatively skewed and heavier tailed. This is consistent with the influence of the hafnia heterogeneities contributing to the heavy tails in modulus/hardness distributions that correspond to the softest, weakly bonded regions probed across microstructures. Despite this heterogeneity, each cumulative distribution (Fig. 12*c-d*) contains a single dominant peak; the shift in these peaks towards greater nanohardness as the compositions approached 50/50 vol% indicates that solid solution strengthening dominates the mechanical behavior of the microstructure over the weaker influence of softer heterogeneities.

The variation of bulk strength, microstructure, and nanohardness was compared as a function of HfC vol% in Fig. 13. To quantify the relative extent of elastic and plastic deformation during indentation, the elastic recovery index is applied and reflects the relative displacement from elastic recovery after peak loading. [55] Despite the limited density of the ternary components, the higher resistance to elastoplastic deformation, greater extent of nanoscale elasticity (recovery index), and higher flexural strengths all suggest stronger bonding in the ternary alloys. These compositions all contained hafnia and had carbon diffuse from the matrix upon cooling. The consistency of improved properties across various length scales for the 50 vol% HfC composition establishes

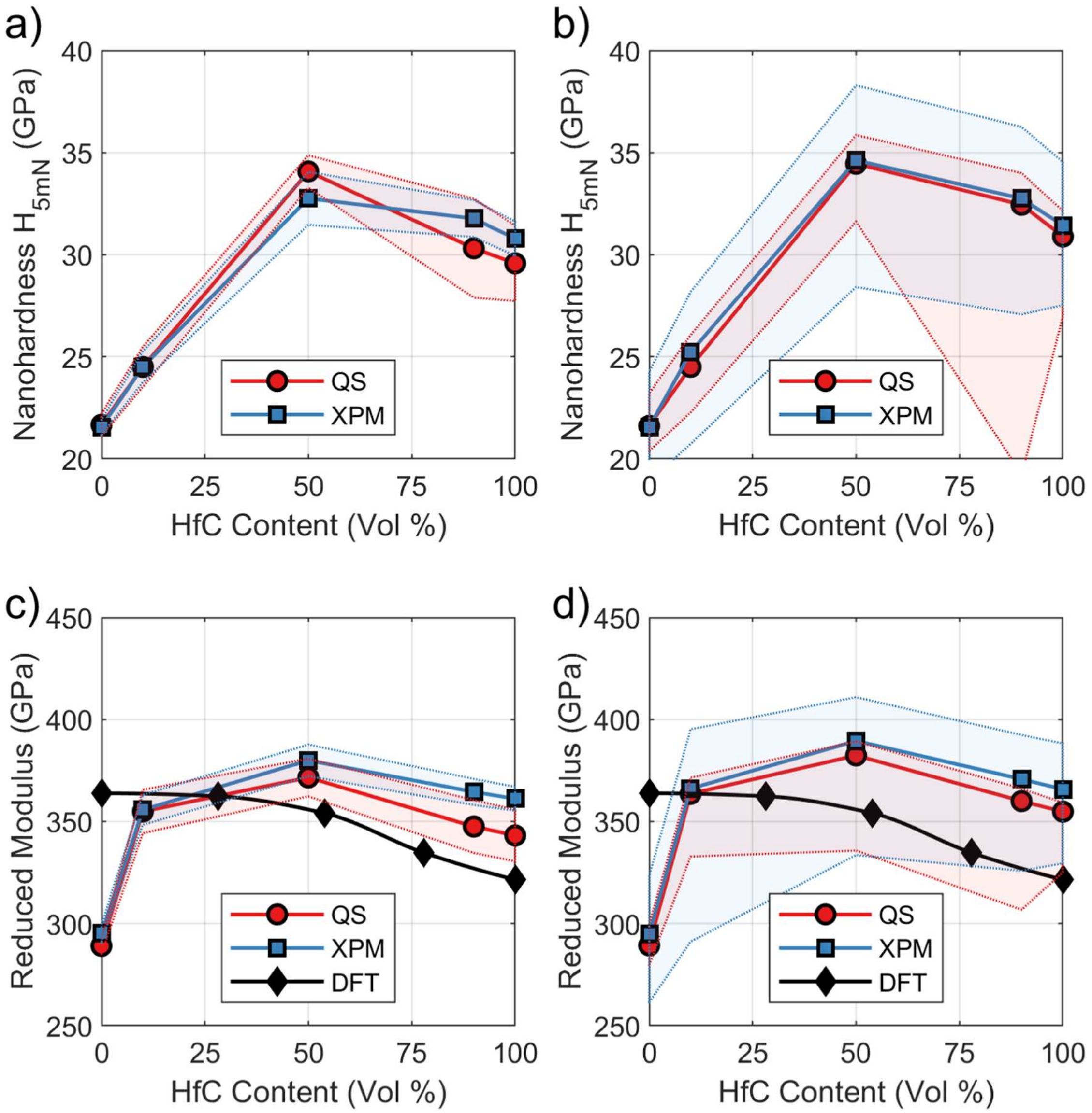

Fig. 11. a) Parametric and b) non-parametric comparisons of QS (quasi-static) and XPM (accelerated-property mapping) validated nanohardness; c) parametric and d) non-parametric comparison of reduced modulus as a function of relative HfC volume fraction, and DFT results from Kim et al. [46] Parametric quantities represent averages bounded by 95 % confidence intervals; nonparametric quantities represent medians bounded by the 90th/10th percentiles.

the motivation to further develop this HfC-TaC alloy for extreme thermomechanical environments. Thus, the 10–50 vol% HfC compositional window yields enhanced fracture properties due to stronger bonding from solid solution strengthening and provides the greatest opportunities to leverage for the development of next-generation ceramic materials for extreme environments.

4. Conclusions

Five compositions of the ternary TaC-HfC were processed via FAST without sintering aids and fabricated under identical time-temperature histories to evaluate structural and mechanical differences driven primarily by compositional and microstructural attributes. The research effort's primary conclusions are the following:

- The measured oxygen content increased with increasing HfC content, acting as a grain refiner and/or grain boundary pinner because of trace oxide phases present. In addition, the driving force for outward carbon diffusion towards the grain boundaries and away from the matrix during sintering was observed to be the greatest for the 50/50 vol% composition. As a result, the solid-solution samples achieved lower relative densities when compared to the pure HfC and TaC endmembers.
- Despite lower densities, the bulk mechanical flexure strength, hardness, and stiffness for ternary solid solution compositions was greater than that for the HfC and TaC endmembers, in agreement with established literature which reported increased bond strength for ternary compositions of the Ta-Hf-C system. Of the compositions studied, TaC had the lowest strength (Weibull parameters), stiffness, and hardness, despite the greatest density and least oxygen content.
- Nanomechanical testing revealed stiffness of HfC-containing samples was substantially greater than expected from DFT calculations, while that of TaC was considerably lower. Although modeling suggests that TaC should be the stiffest composition, experimental conditions, including non-stoichiometry of carbon, the presence of oxygen, and solid-solution strengthening were the key mechanisms influencing the observed mechanical response.
- Relative to the rule-of-mixtures from the pure endmembers, the maximum increase in mechanical property enhancement was systematically seen for compositions containing between 10 and 50 vol

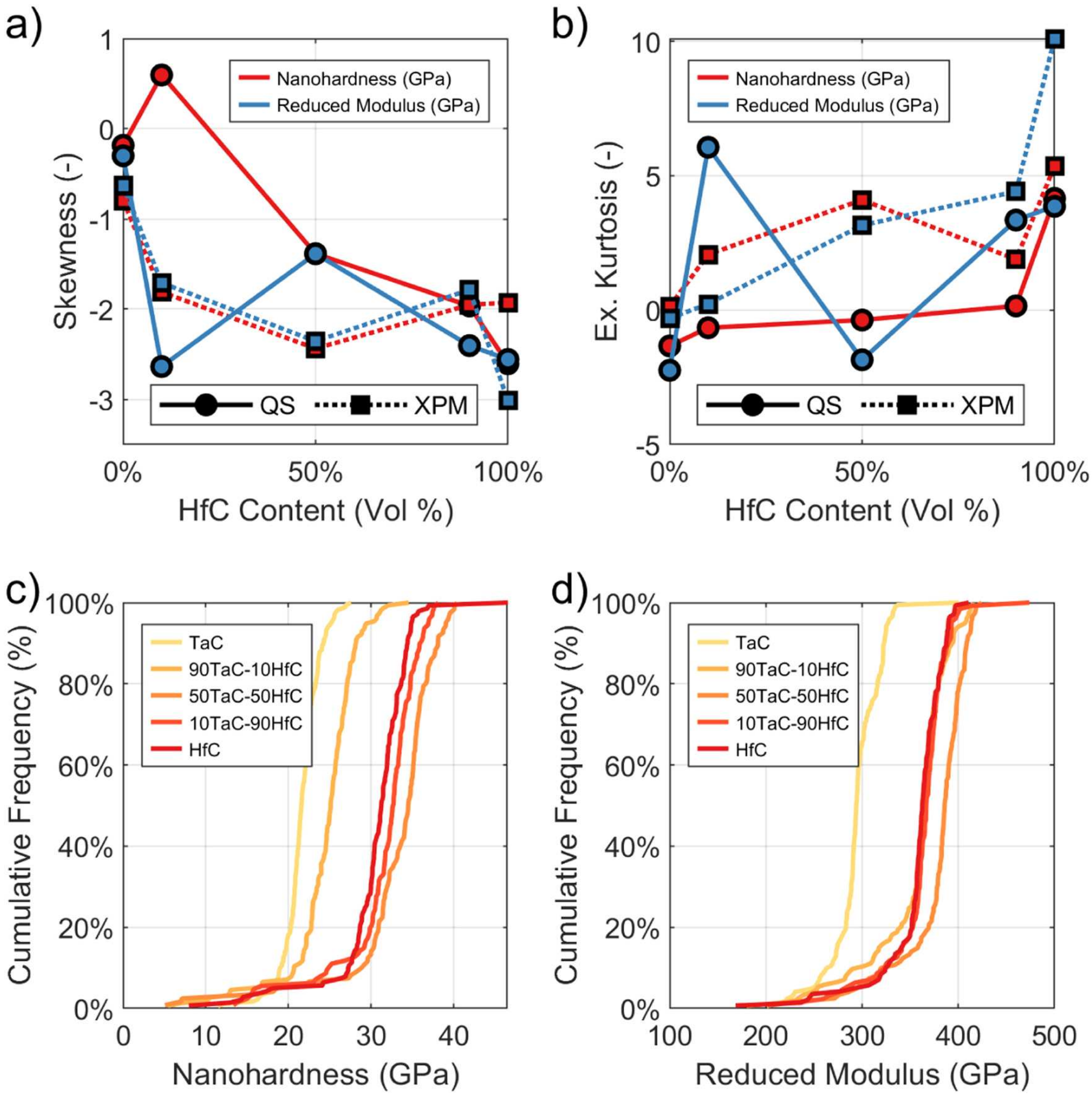

Fig. 12. a) Skewness and b) excess kurtosis comparisons of nanohardness and reduced modulus as a function of relative HfC volume fraction, and c) Pooled nanohardness and d) reduced modulus EDF comparisons of the HfC-TaC compositional effect on the observed nanoindentation mechanical properties.

% HfC, with the peak property enhancement lying at the 50 vol% solid-solution sample. This provides the compositional window for optimizing HfC-TaC alloys for maximum thermomechanical performance and oxide stability in extreme, high temperature environments.

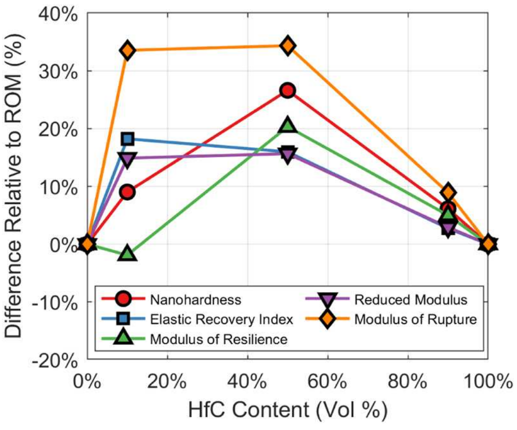

Fig. 13. Comparisons of correlated HfC-TaC mechanical property changes as a function of HfC content. Plotted values represent the average percent changes relative to the arithmetic rule-of-mixture (ROM) endmember HfC/TaC properties.

CRediT authorship contribution statement

Erik T. Furton: Conceptualization, Data curation, Formal analysis, Investigation, Validation, Visualization, Writing – original draft, Writing – review & editing. **Ryan Sweny:** Data curation, Formal analysis, Investigation. **Patrick Albert:** Conceptualization, Data curation, Formal analysis, Project administration, Supervision, Writing – original draft, Writing – review & editing. **Caillin J. Ryan:** Data curation, Formal analysis, Supervision, Writing – original draft, Writing – review & editing. **Ryan Crealese:** Data curation. **Allison M. Beese:** Supervision, Validation, Writing – review & editing. **Douglas E. Wolfe:** Supervision, Writing – review & editing. **Michael P. Galaini:** Data curation, Formal analysis, Investigation. **Petr A. Kolonin:** Data curation, Formal analysis, Investigation.

Declaration of Competing Interest

The authors declare that they have no known competing financial interests or personal relationships that could have appeared to influence the work reported in this paper.

Acknowledgments and support

We would like to gratefully acknowledge the internal development funding from The Applied Research Laboratory at The Pennsylvania State University for their financial support of this work. The financial support provided by the National Science Foundation through award number CMMI-1652575 and the National Science Foundation Graduate Research Fellowship under Grant No. DGE1255832 is gratefully acknowledged.

References

[1] D. Sziroczak, H. Smith, A review of design issues specific to hypersonic flight vehicles, Prog. Aerosp. Sci. *84* (2016) 1–28, https://doi.org/10.1016/j.paerosci.2016.04.001.

[2] A. Purwar, B. Basu, Thermo-structural design of ZrB2–SiC-based thermal protection system for hypersonic space vehicles, J. Am. Ceram. Soc. *100* (4) (2017) 1618–1633.

[3] M. Ferraiuolo, C. Palumbo, A. Sellitto, A. Riccio, Investigating the thermo-mechanical behavior of a ceramic matrix composite wing leading edge by sub-modeling based numerical analyses, Computation *8* (2) (2020) 22, https://doi.org/10.3390/computation8020022.

[4] J. Sun, Qingyong Zhu, A physical model for solving the dredging thermal protection system of hypersonic vehicle leading edge, AIP Adv. *9* (2) (2019) 025203, https://doi.org/10.1063/1.5083820.

[5] K.M. Hanquist, I.D. Boyd, Plasma assisted cooling of hot surfaces on hypersonic vehicles, Front. Phys. *7* (2019) 9, https://doi.org/10.3389/fphy.2019.00009.

[6] F. Monteverde, R. Savino, M.D.S. Fumo, A. Di Maso, Plasma wind tunnel testing of ultra-high temperature ZrB2–SiC composites under hypersonic re-entry conditions, J. Eur. Ceram. Soc. *30* (11) (2010) 2313–2321, https://doi.org/10.1016/j.jeurceramsoc.2010.01.029.

[7] M.M. Opeka, I.G. Talmy, J.A. Zaykoski, Oxidation-based materials selection for 2000 °C + hypersonic aerosurfaces: theoretical considerations and historical experience, J. Mater. Sci. *39* (19) (2004) 5887–5904, https://doi.org/10.1023/B:JMSC.0000041686.21788.77.

[8] Hernandez, J.; Fouliard, Q.; Anderson, C.; Northam, M.; Vo, K.; Clabaugh, J.; Wolfe, D.; Aimer, J.; Park, J.S.; Ghosh, R. In-Situ Xrd Characterization of Multilayered Ceramic Composite Systems for Hypersonic Applications. In 23rd AIAA International Space Planes and Hypersonic Systems and Technologies Conference, 2020; American Institute of Aeronautics and Astronautics Inc, AIAA, 2020.

[9] T.H. Squire, J. Marschall, Material property requirements for analysis and design of UHTC components in hypersonic applications, J. Eur. Ceram. Soc. *30* (11) (2010) 2239–2251, https://doi.org/10.1016/j.jeurceramsoc.2010.01.026.

[10] D.M. Van Wie, D.G. Drewry Jr., D.E. King, C.M. Hudson, The hypersonic environment: required operating conditions and design challenges, J. Mater. Sci. *39* (19) (2004) 5915–5924, https://doi.org/10.1023/B:JMSC.0000041688.68135.8b.

[11] Walker, S.; Sullivan, B. Sharp Refractory Composite Leading Edges on Hypersonic Vehicles. In 12th AIAA International Space Planes and Hypersonic Systems and Technologies; American Institute of Aeronautics and Astronautics: Norfolk, Virginia, 2003. https://doi.org/10.2514/6.2003-6915.

[12] Silvestroni, L.; Sciti, D. Mechanical Properties: A Comparison among Pressureless Sintered Ultra-Refractory Carbides. 2010, 2010 (1994). https://doi.org/10.1155/2010/835018.

[13] I. Shabalin, Ultra-High Temperature Materials I, Springer Science+Business Media, Dordrecht, 2014.

[14] N.S. Karthiselva, B.S. Murty, S.R. Bakshi, Low temperature synthesis of dense and ultrafine grained zirconium diboride compacts by reactive spark plasma sintering, Scr. Mater. *110* (2016) 78–81, https://doi.org/10.1016/j.scriptamat.2015.08.005.

[15] O. Cedillos-Barraza, D. Manara, K. Boboridis, T. Watkins, S. Grasso, D. D. Jayaseelan, R.J.M. Konings, M.J. Reece, W.E. Lee, Investigating the highest melting temperature materials: a laser melting study of the TaC-HfC system, Sci. Rep. *6* (1) (2016) 37962, https://doi.org/10.1038/srep37962.

[16] E. Castle, T. Csanádi, S. Grasso, J. Dusza, M. Reece, Processing and properties of high-entropy ultra-high temperature carbides, Sci. Rep. *8* (1) (2018) 8609, https://doi.org/10.1038/s41598-018-26827-1.

[17] Zhang, C.High Temperature Oxidation Study of Tantalum Carbide-Hafnium Carbide Solid Solutions Synthesized by Spark Plasma Sintering. Doctor of Philosophy Materials Science and Engineering, Florida International University, 2016. https://doi.org/10.25148/etd.FIDC001239.

[18] Y. Pan, P. Zhou, Y. Peng, Y. Du, F. Luo, A thermodynamic description of the C–Hf–Ta system over the whole composition and temperature ranges, Calphad *53* (2016) 1–9, https://doi.org/10.1016/j.calphad.2016.02.001.

[19] J. Zhang, S. Wang, W. Li, Y. Yu, J. Jiang, Understanding the oxidation behavior of Ta–Hf–C ternary ceramics at high temperature, Corros. Sci. *164* (2020) 108348, https://doi.org/10.1016/j.corsci.2019.108348.

[20] M. Sanchez, K.A. Acord, S. Frueh, L.M. Rueschhoff, O.A. Graeve, Phase transitions and oxidation behavior during oxyacetylene torch testing of TaC–HfC solid solutions, Adv. Eng. Mater. *25* (18) (2023) 2300138, https://doi.org/10.1002/adem.202300138.

[21] Y. Yang, J.H. Perepezko, C. Zhang, Oxidation synthesis of Hf6Ta2O17 superstructures, Mater. Chem. Phys. *197* (2017) 154–162, https://doi.org/10.1016/j.matchemphys.2017.04.055.

[22] Gaballa, O.G. Processing Development of 4TaC-HfC and Related Carbides and Borides for Extreme Environments. 2012.

[23] S.A. Ghaffari, M.A. Faghihi-Sani, F. Golestani-Fard, S. Ebrahimi, Pressureless sintering of Ta0.8Hf0.2C UHTC in the Presence of MoSi2, Ceram. Int. *39* (2) (2013) 1985–1989, https://doi.org/10.1016/j.ceramint.2012.08.050.

[24] Z. Zhang, S. Fu, F. Aversano, M. Bortolotti, H. Zhang, C. Hu, S. Grasso, Arc Melting: a novel method to prepare homogeneous solid solutions of transition metal carbides (Zr, Ta, Hf), Ceram. Int. *45* (7) (2019) 9316–9319, https://doi.org/10.1016/j.ceramint.2019.01.238.

[25] O. Gaballa, B. a Cook, a M. Russell, Reduced-temperature processing and consolidation of ultra-refractory Ta4HfC5, Int. J. Refract. Met. Hard Mater. *41* (2013) 293–299, https://doi.org/10.1016/j.ijrmhm.2013.04.018.

[26] L. Silvestroni, A. Bellosi, C. Melandri, D. Sciti, J.X. Liu, G.J. Zhang, Microstructure and properties of HfC and TaC-based ceramics obtained by ultrafine powder, J. Eur. Ceram. Soc. *31* (4) (2011) 619–627, https://doi.org/10.1016/j.jeurceramsoc.2010.10.036.

[27] L. Silvestroni, D. Sciti, Transmission electron microscopy on Hf- and Ta-Carbides sintered with TaSi2, J. Eur. Ceram. Soc. *31* (15) (2011) 3033–3043, https://doi.org/10.1016/j.jeurceramsoc.2011.07.003.

[28] D.V. Quach, J.R. Groza, A. Zavaliangos, U. Anselmi-Tamburini, Fundamentals and applications of field/current assisted sintering, in: Sintering of Advanced Materials, Elsevier, 2010, pp. 249–275e, https://doi.org/10.1533/9781845699949.2.249.

[29] Spark Plasma Sintering of Materials: Advances in Processing and Applications; Cavaliere, P., Ed.; Springer International Publishing: Cham, 2019. https://doi.org/10.1007/978–3-030–05327-7..

[30] S.-K. Sun, G.-J. Zhang, W.-W. Wu, J.-X. Liu, T. Suzuki, Y. Sakka, Reactive spark plasma sintering of ZrC and HfC ceramics with fine microstructures, Scr. Mater. *69* (2) (2013) 139–142, https://doi.org/10.1016/j.scriptamat.2013.02.017.

[31] D. Sciti, M. Nygren, Spark plasma sintering of ultra refractory compounds, J. Mater. Sci. *43* (19) (2008) 6414–6421, https://doi.org/10.1007/s10853-008-2718-7.

[32] A. Nino, T. Hirabara, S. Sugiyama, H. Taimatsu, Preparation and characterization of tantalum carbide (TaC) ceramics, Int. J. Refract. Met. Hard Mater. *52* (2015) 203–208, https://doi.org/10.1016/j.ijrmhm.2015.06.015.

[33] E. Khaleghi, Y.-S. Lin, M.A. Meyers, E.A. Olevsky, Spark plasma sintering of tantalum carbide, Scr. Mater. *63* (6) (2010) 577–580, https://doi.org/10.1016/j.scriptamat.2010.06.006.

[34] A. Nisar, S. Ariharan, K. Balani, Densification kinetics and mechanical properties of tantalum carbide, Int. J. Refract. Met. Hard Mater. *73* (2018) 221–230, https://doi.org/10.1016/j.ijrmhm.2018.02.013.

[35] S.R. Bakshi, V. Musaramthota, D. Lahiri, V. Singh, S. Seal, A. Agarwal, Spark plasma sintered tantalum carbide: effect of pressure and nano-boron carbide addition on microstructure and mechanical properties, Mater. Sci. Eng.: A *528* (3) (2011) 1287–1295, https://doi.org/10.1016/j.msea.2010.10.009.

[36] L. Liu, G. Geng, Y. Jiang, Y. Wang, W. Hai, W. Sun, Y. Chen, L. Wu, Microstructure and mechanical properties of tantalum carbide ceramics: effects of Si3N4 as sintering aid, Ceram. Int. *43* (6) (2017) 5136–5144, https://doi.org/10.1016/j.ceramint.2017.01.028.

[37] D. Demirskyi, H. Borodianska, T. Nishimura, T. Suzuki, K. Yoshimi, O. Vasylkiv, Deformation- Resistant Ta0.2Hf0.8C solid- solution ceramic with superior flexural strength at 2000 °C, J. Am. Ceram. Soc. *105* (1) (2022) 512–524.

[38] O. Guillon, J. Gonzalez-Julian, B. Dargatz, T. Kessel, G. Schierning, J. Räthel, M. Herrmann, Field-assisted sintering technology/spark plasma sintering: mechanisms, materials, and technology developments, Adv. Eng. Mater. *16* (7) (2014) 830–849, https://doi.org/10.1002/adem.201300409.

[39] D.E. Wolfe, P.E. Albert, C.J. Ryan, J.A. Reiss, S.P. Stepanoff, P.A. Kolonin, Optimized processing of high density ternary hafnium-tantalum carbides via field assisted sintering technology for transition into hypersonic applications, J. Eur. Ceram. Soc. *42* (2) (2022) 327–335, https://doi.org/10.1016/j.jeurceramsoc.2021.10.014.

[40] ASTM International. E112–13: Test Methods for Determining Average Grain Size. https://doi.org/10.1520/E0112–13R21.

[41] ASTM International. E1941–10: Test Method for Determination of Carbon in Refractory and Reactive Metals and Their Alloys by Combustion Analysis; ASTM International. https://doi.org/10.1520/E1941–10R16.

[42] ASTM International. E1409–13: Test Method for Determination of Oxygen and Nitrogen in Titanium and Titanium Alloys by Inert Gas Fusion. https://doi.org/10.1520/E1409–13R21.

[43] Khalili, A.; Kromp, K. Statistical Properties of Weibull Estimators. *Statistical properties of Weibull estimators* 1991, 26, 6741–6752.

[44] DeSalvo, G.J. Theory and Structural Design Applications of Weibull Statistics; WANL-TME-2688; Westinghouse Electric Corp: Pittsburgh, PA, 1970; p WANL-TME–2688, 4120627. http://www.osti.gov/servlets/purl/4120627-2LlYKs/ (accessed 2023-09-26).

[45] W.C. Oliver, G.M. Pharr, An improved technique for determining hardness and elastic modulus using load and displacement sensing indentation experiments, J. Mater. Res. *7* (1992) 1564–1583, https://doi.org/10.1557/JMR.1992.1564.

[46] J. Kim, H. Kwon, B. Kim, Y.J. Suh, Finite temperature thermal expansion and elastic properties of (Hf1-xTax)C ultrahigh temperature ceramics, Ceram. Int. *45* (8) (2019) 10805–10809, https://doi.org/10.1016/j.ceramint.2019.02.155.

[47] A.I. Gusev, A.N. Zyryanova, Ordering and magnetic susceptibility of non-stoichiometric hafnium carbide, *Phys. Stat. Sol. (a) 177* (419) (2000).

[48] R.J. Fries, L.A. Wahman, Effect of Stoichiometry on the Thermal Expansion of TaCx, J. Am. Ceram. Soc. *50* (9) (1967) 475–477, https://doi.org/10.1111/j.1151-2916.1967.tb15165.x.

[49] X. Zhang, G.E. Hilmas, W.G. Fahrenholtz, D.M. Deason, Hot pressing of tantalum carbide with and without sintering additives, J. Am. Ceram. Soc. *90* (2) (2007) 393–401, https://doi.org/10.1111/j.1551-2916.2006.01416.x.

[50] Dinsdale, A.T. SGTE data for pure elements.

[51] S.J. McCormack, K. Tseng, R.J.K. Weber, D. Kapush, S.V. Ushakov, A. Navrotsky, W.M. Kriven, In-situ Determination of the HfO_2–Ta_2O_5-temperature phase diagram up to 3000 °C, J. Am. Ceram. Soc. *102* (8) (2019) 4848–4861, https://doi.org/10.1111/jace.16271.

[52] J. Wang, H.P. Li, R. Stevens, Hafnia and Hafnia-toughened ceramics, J. Mater. Sci. *27* (20) (1992) 5397–5430, https://doi.org/10.1007/BF00541601.

[53] ASTM International. C1239–06: Standard Practice for Reporting Uniaxial Strength Data and Estimating Weibull Distribution Parameters for Advanced Ceramics, 2017.

[54] J. Gong, Y. Li, Relationship between the estimated weibull modulus and the coefficient of variation of the measured strength for ceramics, J. Am. Ceram. Soc. *82* (2) (2004) 449–452, https://doi.org/10.1111/j.1551-2916.1999.tb20084.x.

[55] A.M. Okoro, R. Machaka, S.S. Lephuthing, S.R. Oke, M.A. Awotunde, P. A. Olubambi, Nanoindentation studies of the mechanical behaviours of spark plasma sintered multiwall carbon nanotubes reinforced Ti6Al4V nanocomposites, Mater. Sci. Eng.: A *765* (2019) 138320, https://doi.org/10.1016/j.msea.2019.138320.